Optimized Design of a Coupled-Inductor Buck Converter, 48 to 12 V, 1 kW, Using Planar Magnetics and GaN-FETs for MHz-Range Operation

Track 6. Vehicle Electrification-related Technologies

Abstract—**The next generation of automotive vehicles and datacenters requires highly compact and efficient 48 V to 12 V point-of-load converters. This paper investigates the impact of coupling on the electrical properties of 2-phase buck converters operating in triangular current mode to achieve soft-switching. A novel planar inductor geometry with four poles and distributed air-gaps for operation beyond 1 MHz is presented that minimizes copper-losses from external proximity effect. An experimental prototype with 1 kW output achieves an impressive power density of 80 kW/l (1300 W/in³) and a peak efficiency of 96.5 %, demonstrating the efficacy of the inductor structure.**

Index Terms—**coupled inductor, magnetic integration, planar inductor, triangular current mode**

I. INTRODUCTION

With a growing power demand, power distribution in both conventional and electric vehicles presents an increasing challenge. Traditionally, $12\,\text{V}$ are used to distribute the power to all auxiliary devices which requires large cable diameters. Recently, many researchers proposed a $48\,\text{V}$ distribution bus to reduce the cost of the wire assembly and/or reduce losses CITE. As most devices are still operating at $12\,\text{V}$, highly compact and efficient point-of-load converters are required. This conversion stage is a critical part of distributed power architectures and its performance has a direct impact on system-level efficiency, thermal design, and spatial constraints.

This motivates the use of wide-bandgap semiconductors which offer lower $R_{ds,on}$ and faster switching speeds compared to traditional Si-devices. By increasing the switching frequency, magnetic components and filters can be shrunk significantly enabling very high power densities. Beyond $500\,\text{kHz}$ hard-switched converters are generally unsuitable due to their large switching losses CITE. A lot of research has been done on resonant converters due to their high efficiency and compact design but those are unsuitable when a regulated output voltage is required over a wide input voltage range CITE.

The two phase coupled-inductor buck converter is a promising topology for these applications.
Blabla

II. COUPLED INDUCTOR BUCK CONVERTER IN TCM

A. Working principle

The topology of the two phase coupled-inductor buck converter is shown in figure 1. By integrating both inductors on
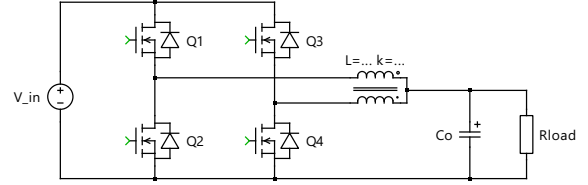

Fig. 1: Schematic of the Coupled Inductor Buck Converter.

the same core, the inductor volume can be shrunk significantly while the modulation remains the same: Both legs are switched $180\,\text{deg}$ out of phase. If the ripple is more than twice the phase current, the leg current becomes negative prior to the rising edge of each leg resulting in a zero voltage switching (ZVS) turn-on of all transistors. Only the small turn-off losses are observed now. This mode is called triangular current mode (TCM) [1].

B. Impact of the Coupling Factor

The symmetrical coupled inductor consists of two identical coils that are wound in a way, that the flux of one coil links with the flux of the second coil and vice versa with both coils connected on one side. This configuration can be described mathematically using

$$\begin{bmatrix} v_a \\ v_b \end{bmatrix} = \begin{bmatrix} 1 & k \\ k & 1 \end{bmatrix} L_{self} \begin{bmatrix} \frac{di_1}{dt} \\ \frac{di_2}{dt} \end{bmatrix} \tag{1}$$

with self-inductance L_{self} and coupling-factor k. Note that k can be positive or negative; the impact of that will be analyzed later. In order to simplify the equations and provide a more intuitive understanding, the equivalent circuit in figure TODO is introduced. Both circuits are electrically equivalent for

$$\begin{aligned} L_{out} &= (1+k)\frac{L_{self}}{2} \\ L_m &= (1-k)\frac{L_{self}}{2}. \end{aligned} \tag{2}$$

The voltage at the virtual central node is now only dependent of the two leg voltages v_1 and v_2 decoupling the governing

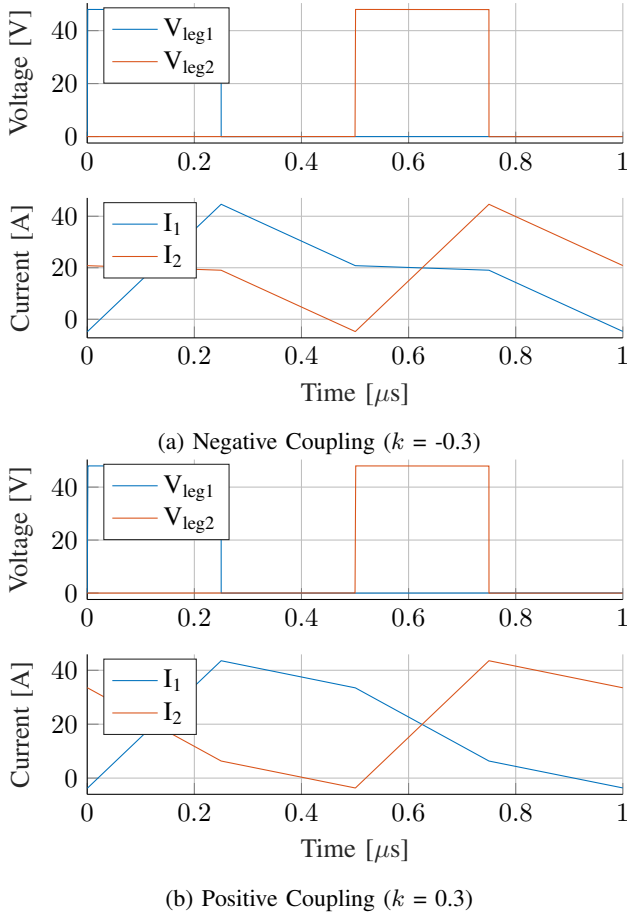(a) Negative Coupling (k = -0.3)

(b) Positive Coupling (k = 0.3)

Fig. 2: Waveforms for positive and negative coupling. It can be seen that the slopes are changed but the behavior in the vicinity of the switching instances is fundamentally the same. ToDo: Make smaller!

equations:

$$\frac{di_{out}}{dt} = \frac{1}{L_{out}}\left(\frac{v_1 + v_2}{2} - v_{out}\right)$$
$$\frac{di_m}{dt} = \frac{1}{L_{out}}\left(\frac{v_1 - v_2}{2}\right) \tag{3}$$
$$\text{with} \quad i_{out} = i_1 + i_2 \quad \text{and} \quad i_m = i_1 - i_2$$

From this, the differential equations for each interval can be easily calculated and afterwards the important converter parameters. An effective dutycycle D_{eff} can be introduced with $D_{eff} = D$ for $D \le 0.5$ and $D_{eff} = 1 - D$ for $D > 0.5$. The output ripple is given by

$$\frac{2V_{in}}{f_s(1+k)L_{self}}D_{eff}\left(\frac{1}{2} - D_{eff}\right). \tag{4}$$

The ripple in each leg which is important for soft-switching is

$$\Delta I_{leg} = \frac{V_{in}D_{eff}}{2f_sL_{self}}\left(\frac{2}{1+k}(0.5 - D_{eff}) + \frac{1}{1-k}\right). \tag{5}$$

Both are shown in figure 3. There is a strong dependency of these parameters with dutycycle but interestingly, the leg ripple
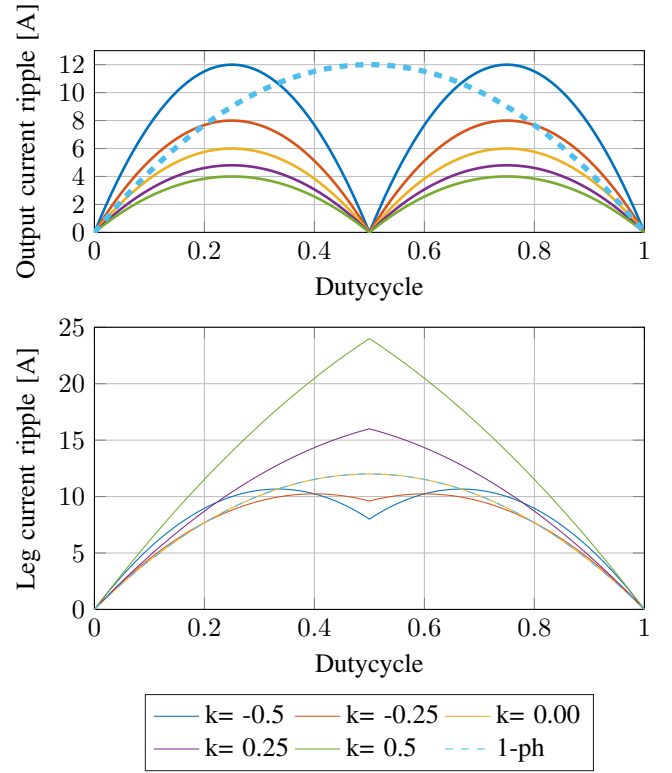

Fig. 3: Output current ripple and leg ripple for different coupling factors and constant input voltage. 1-ph for comparison. ToDo: Redo with normalized y-axis.

(a) Double-PQ
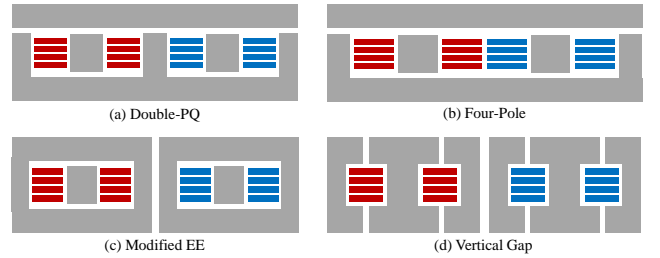
(b) Four-Pole

(c) Modified EE

(d) Vertical Gap

Fig. 4: Structure of the cores; Cut through the center, sie-view. First winding in red, second winding in blue.

current is not that significantly influenced by the coupling-factor. As the coupling increases, L_{out} increases while L_m decreases causing a decrease in i_{out} but an increase in i_m.

As mentioned before, for soft-switching I_{on} needs to be negative and generally needs to be below a certain value to guarantee a sufficiently short dead time which can be written as $\Delta I_{leg} \ge i_{out} + 2I_{on,max}$. This is fulfilled for

$$f_s < \frac{V_{in}D_{eff}}{2L_{self}(i_{out} + 2I_{on,max})}\left(\frac{2}{1+k}(0.5 - D_{eff}) + \frac{1}{1-k}\right). \tag{6}$$

III. INDUCTOR DESIGN

A. Inductor geometry

Four different geometries, two coupled, and two uncoupled ones for reference, were considered for this application as shown in figure 6. The Double-PQ structure was introduced by [2] and modified with a dual air-gap; more on that later. The four-pole structure is very similar but omits the central pole which creates separate paths for DC and fundamental flux [3]. The third geometry is basically an EE-Core but instead of one central gap two gaps are used. Lastly, a vertical gap geometry is investigated which can partly compensate the internal proximity effect [4].

All designs use a single turn with all layers in parallel. Designs with more than one turn were not considered because the desired inductance and coupling-factor could not be achieved in that case due to fringing.

B. Material limitations

High-frequency ferrite materials for power applications have some unique properties that differ from those for lower frequency applications. TDK's PC200 was selected for this design as it exhibits very low loss in the range of 1 to 4 MHz. However, the performance of PC200 significantly degrades for a field strength $H_{dc} > 50$ A/m and at $H_{dc} > 100$ A/m its losses double [5]. Therefore, the inductor was designed with a maximum H_{dc} of 40 A/m to have some margin.

C. Positive vs negative coupling

From figure 3 there is no clear winner between positive and negative coupling. From the point of inductor design however, there is a very notable difference in the DC-flux distribution: For negative coupling, it is distributed very uniformly across the core resulting in a low peak field strength. For positive coupling, the DC-flux circulates between the two pillars resulting in a large imbalance in DC-flux between the inner and outer part of the core as shown in figure 5. The peak field strength is much higher and as the core has to be designed with respect to the H_{dc} limit, this means thick top and bottom even though this area is not needed on the outside. As a result, the core gets much larger without having a performance improvement. Therefore, negative coupling is clearly the better choice.

D. Simulation Process

For the simulation, the open-source 2D FEM software FEMM was used due to its high speed and easy integration with Matlab. As the core-structures are neither planar nor axisymmetric, the designs were first transformed to a planar structure. All cross-sectional areas are kept the same and the depth of the design is determined by the length of the winding[1].

For validation, the design was also transformed into an axisymmetric structure (neglecting the effects of coupling). This

---

[1]As the current does not flow in the middle of the winding but closer to its center due to the shorter length and the magnetic field, the circumference taken not from the middle of the winding but closer to the inside
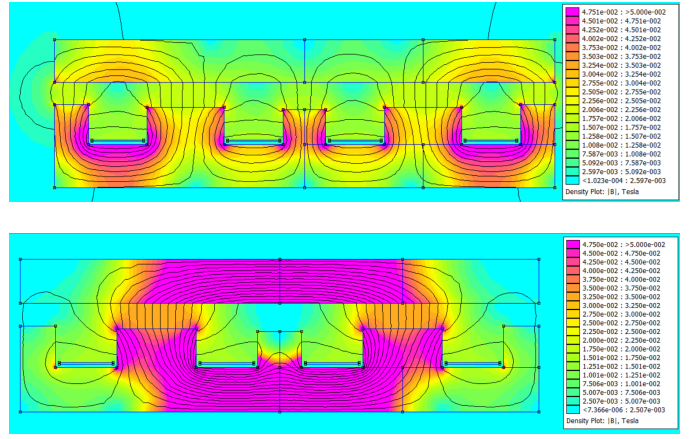

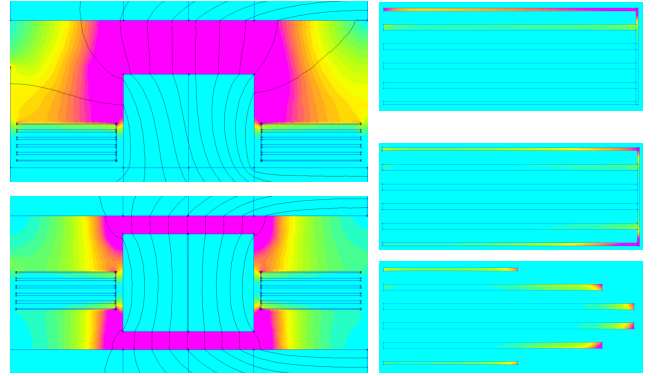Fig. 5: DC-Flux for negative coupling (top) and positive coupling (bottom).

Fig. 6: Comparison of convential air-gap with the optimized version. Because all layers are in parallel the current crowds in areas of large field-strength. By splitting the gap, the field gets distributed more evenly and the current distribution improves. Utilizing a smaller width for the outer layers, i.e. moving the copper away from the high-flux areas distributes the current even better.

has the advantage that the current distribution and consequently copper-loss is closer to reality at the expense of less-precise core-loss.

E. Split air-gap and optimized windings

The external proximity effect caused by the air-gap plays an important role for the current distribution and consequently the losses of this high-frequency inductor. The field-strength at the top of the windings is large and almost zero at the bottom.

TABLE I: Comparison of the size and loss of the optimized pillar and windings for the four-pole design.

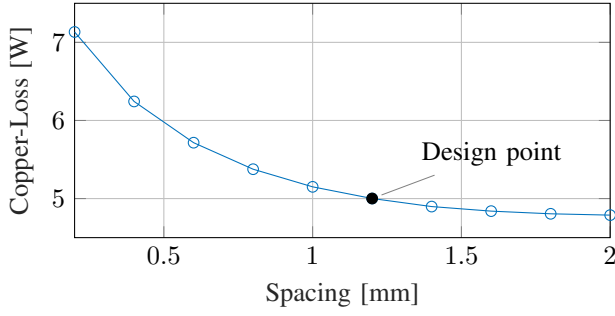|	Volume [cm^3]	Copper Loss [W]
Original design	5.8	7.0
Air-Gap on top and bottom	5.5	5.7
Air-Gap on top and bottom, curved windings	5.3	5.0

Fig. 7: Spacing between PCB and core vs. loss for the four-pole core (with curved windings and centered pillar). The distance between the PCB and the side air-gap core is fixed to $0.2\,\mathrm{mm}$ and the distance between PCB and bottom is varied. The pillar is always centered between top and bottom.

As a result, the AC current is only flowing in the top layers. By centering the pillar vertically in the window such that there is an equal air-gap on the top and on the bottom, the field-strength is distributed much more uniformly and current flows in the top and bottom layers. This results in a $20\,\%$ reduction in losses, which can be reduced even further by using curved windings as shown in table I.

F. Inductor Design Process

Using a brute-force algorithm was deemed impossible due to the many free variables with the custom design. Instead, a manual optimization was conducted for each structure. The desired switching-frequency was fixed to $1.5\,\mathrm{MHz}$ for full-load operation, the coupling-factor to -0.3, and the winding with to $3\,\mathrm{mm}$ as this showed a good balance between size and losses. The cross-sectional areas were designed to result in $H_{dc} \leq 40\,\mathrm{A/m}$ and the air-gaps are defined by desired inductance (i.e. switching frequency) and coupling-factor. The spacing between printed circuit board (PCB) and top/bottom of the core is the only free variable and has to be chosen for a compromise between size and efficiency.

G. Vertical Air-Gap

The design with vertical air-gap showed a significantly lower loss compared to a traditional horizontal gap while having a much lower volume. This confirms the results from [4]. The main downside of this design is the significant external field on top and bottom of the inductor. This makes cooling difficult as no conductive material can be placed on top or bottom of the core, eliminating one of the typical advantages of planar inductors: The large area for cooling. Cooling from the side is proposed by [4] by having copper extending to the outside of the core where a heatsink can be attached but this is much less convenient and requires additional space.

H. Comparison of Core Structures

A comparison of the core structures is shown in table II. All designs except the one with vertical gap use the optimized curved windings. The four-pole structure showed the lowest losses and and volume.

TABLE II: Comparison of the size and loss of the different core structures for $1.5\,\mathrm{MHz}$ respecting the H_{dc} limit.

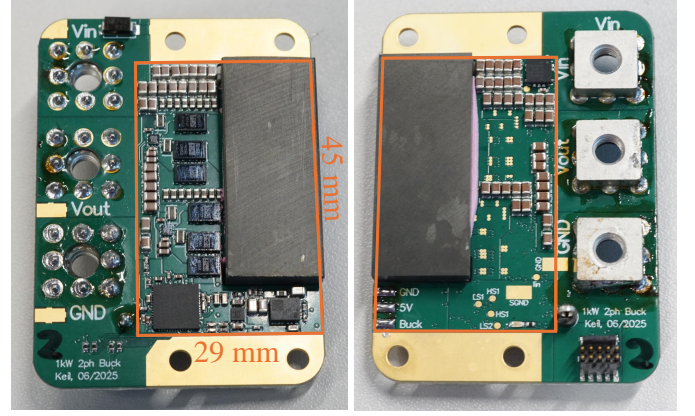|	Total Area [cm^2]	Height [cm]	Volume [cm^3]	Copper Loss [W]
Four-Pole	5.5	0.9	5.3	5.0
Double PQ	6.2	0.9	5.5	5.2
Vertical gap	8.0	0.7	5.8	5.6
UU core	8.1	1.1	8.9	6.0

Fig. 8: Fully assembled prototype (without heatspreader). The converter area shown in orange is 45 x 29 x $9.5\,\mathrm{mm}$. Outside of this area only the connectors for power and programming are placed as well as a protection diode and the programming resistors.

IV. EXPERIMENTAL PROTOTYPE

A. Hardware implementation

The assembled prototype is shown in figure 8. It uses Infineon's IGC025S08S1 $80\,\mathrm{V}$ GaN HEMTs and Analog Devices' LT8418 gate drivers. Two parallel low side transistors per phase are used as the converter operates at a low dutycycle. To minimize the stray inductance, the decoupling capacitors for the half-bridges were connected to the devices with a vertical power-loop layout which uses the first inner layer as a return path as proposed by [6]. The whole system is controlled by a TI F280049C real-time microcontroller. Furthermore, the TPSM365R6 integrated buck-converter module is used for the housekeeping power-supply and an Allegro Microsystems ACS37220 monitors the input current. A total of 44 $2.2\,\mu\mathrm{F}$ 0805 $100\,\mathrm{V}$ X7R capacitors are used to stabilize the input voltage resulting in a derated input capacitance of $20\,\mu\mathrm{F}$. This relatively small package was chosen because larger packages exhibit too much inductance causing resonance in the capacitor. At the output, 16 capacitors of the same type with a derated capacitance of $33\,\mu\mathrm{F}$ are used to provide a low-ripple output voltage. Compared to other designs, this converter does not need any additional off-board capacitance.

B. Test results

A more detailed analysis of the losses will be given in the final paper including a calculated contribution of the dielectric volume loss as introduced by [7].

REFERENCES

[1] C. Marxgut, J. Biela, and J. W. Kolar, "Interleaved Triangular Current Mode (TCM) resonant transition, single phase PFC rectifier with high efficiency and high power density," in *The 2010 International Power Electronics Conference - ECCE ASIA* -, Jun. 2010, pp. 1725–1732. [Online]. Available: https://ieeexplore.ieee.org/document/5542048

[2] S. Wang, P. H. Pham, Q. Li, A. Nabih, and P. R. Prakash, "PCB Winding-Based Coupled Inductor for a High-Frequency DC/DC Converter with 99% Efficiency," in *2023 IEEE Applied Power Electronics Conference and Exposition (APEC)*, Mar. 2023, pp. 420–425, iSSN: 2470-6647. [Online]. Available: https://ieeexplore.ieee.org/document/10131439

[3] M. Hua, J. Chen, G. Xu, and H. Wu, "Ultra-thin Coupled Inductor for a GaN-Based CRM Buck Converter," in *2021 IEEE Workshop on Wide Bandgap Power Devices and Applications in Asia (WiPDA Asia)*, Aug. 2021, pp. 138–142. [Online]. Available: https://ieeexplore.ieee.org/document/9656036/citations#citations

[4] J. Schäfer, D. Bortis, and J. W. Kolar, "Novel Highly Efficient/Compact Automotive PCB Winding Inductors Based on the Compensating Air-Gap Fringing Field Concept," *IEEE Transactions on Power Electronics*, vol. 35, no. 9, pp. 9617–9631, Sep. 2020, conference Name: IEEE Transactions on Power Electronics. [Online]. Available: https://ieeexplore.ieee.org/document/8968357

[5] TDK, "High-Frequency, Low-Loss Ferrite Material PC200." [Online]. Available: https://product.tdk.com/de/techlibrary/productoverview/ferrite_pc200.html

[6] D. Reusch and J. Strydom, "Understanding the Effect of PCB Layout on Circuit Performance in a High-Frequency Gallium-Nitride-Based Point of Load Converter," *IEEE Transactions on Power Electronics*, vol. 29, no. 4, pp. 2008–2015, Apr. 2014. [Online]. Available: https://ieeexplore.ieee.org/document/6531683

[7] M. Baumann, C. Drexler, J. Pfeiffer, J. Schueltzke, E. Lorenz, and M. Schmidhuber, "Investigation of core-loss mechanisms in large-scale ferrite cores for high-frequency applications," in *2022 24th European Conference on Power Electronics and Applications (EPE'22 ECCE Europe)*, Sep. 2022, pp. 1–10. [Online]. Available: https://ieeexplore.ieee.org/document/9907281